

# A Novel Calibration Method of Short-Time Waveform Signals Passed through LTI Systems: 1. Methodology and Simple Examples

Masahiro Kitahara<sup>1</sup>, Shoya Matsuda<sup>2</sup>, Yuto Katoh<sup>3</sup>, Hirotsugu Kojima<sup>4</sup>, Yoshiya Kasahara<sup>2</sup>, Yoshizumi Miyoshi<sup>5</sup>, Satoko Nakamura<sup>1</sup>, and Mitsuru Hikishima<sup>6</sup>

<sup>1</sup>Nagoya University

<sup>2</sup>Kanazawa University

<sup>3</sup>Tohoku University

<sup>4</sup>Kyoto University

<sup>5</sup>Institute for Space-Earth Environmental Research, Nagoya University

<sup>6</sup>Institute of Space and Astronautical Science, Japan Aerospace Exploration Agency

November 24, 2022

## Abstract

We propose a novel and accurate calibration method for short-time waveform signals passed through a linear time-invariant (LTI) system that has a non-negligible group delay. Typically, the calibration process of waveform data is expressed by the Fourier transform and is performed in the frequency domain. If the short-time Fourier transform is applied to the waveform data in the calibration process, multiplying the data by a window function is highly recommended to reduce side-lobe effects. However, the multiplied window function is also modified in the calibration process. We analyzed the modification mathematically and derived a novel method to eliminate the modification of the multiplied window function. In the novel method, calibrated data in the frequency domain are inverse-transformed into waveform data at each frequency, divided by a modified window function at each frequency, and accumulated over the frequencies. The principle of this method derived quantitatively indicates that the calibration accuracy depends on the transfer function of the system, frequency resolution of the Fourier transform, type of the window function, and typical frequency of the waveform data. Compared with conventional calibration methods, the proposed method provides more accurate results in various cases. This method is useful for calibration of general radio wave signals through passed LTI systems as well as for calibration of plasma waves observed in space.

1 **A Novel Calibration Method of Short-Time Waveform Signals Passed through**  
2 **LTI Systems: 1. Methodology and Simple Examples**

3  
4 **M. Kitahara<sup>1\*</sup>, S. Matsuda<sup>2</sup>, Y. Katoh<sup>3</sup>, H. Kojima<sup>4</sup>, Y. Kasahara<sup>2</sup>, Y. Miyoshi<sup>1</sup>, S.**  
5 **Nakamura<sup>1</sup>, and M. Hikishima<sup>5</sup>**

6 <sup>1</sup>Institute for Space-Earth Environmental Research, Nagoya University, Nagoya, Japan

7 <sup>2</sup>Graduate School of Natural Science and Technology, Kanazawa University, Kanazawa, Japan

8 <sup>3</sup>Graduate School of Science, Tohoku University, Sendai, Japan

9 <sup>4</sup>Research Institute for Sustainable Humanosphere, Kyoto University, Kyoto, Japan

10 <sup>5</sup>Institute of Space and Astronautical Science/Japan Aerospace Exploration Agency, Kanagawa,  
11 Japan

12 Corresponding author: Masahiro Kitahara ([kitahara.masahiro@isee.nagoya-u.ac.jp](mailto:kitahara.masahiro@isee.nagoya-u.ac.jp))

13  
14 **Key Points:**

- 15 • We propose a novel calibration method using short-time Fourier transform for waveform  
16 data, such as plasma waves observed in space.
- 17 • The accuracy of the novel method is evaluated using the transfer functions of well-known  
18 filters and frequency-fixed sinusoidal waveforms.
- 19 • The novel method provides the most accurately calibrated data compared with  
20 conventional methods using short-time Fourier transform.  
21

## 22 **Abstract**

23 We propose a novel and accurate calibration method for short-time waveform signals  
24 passed through a linear time-invariant (LTI) system that has a non-negligible group delay.  
25 Typically, the calibration process of waveform data is expressed by the Fourier transform and is  
26 performed in the frequency domain. If the short-time Fourier transform is applied to the  
27 waveform data in the calibration process, multiplying the data by a window function is highly  
28 recommended to reduce side-lobe effects. However, the multiplied window function is also  
29 modified in the calibration process. We analyzed the modification mathematically and derived a  
30 novel method to eliminate the modification of the multiplied window function. In the novel  
31 method, calibrated data in the frequency domain are inverse-transformed into waveform data at  
32 each frequency, divided by a modified window function at each frequency, and accumulated  
33 over the frequencies. The principle of this method derived quantitatively indicates that the  
34 calibration accuracy depends on the transfer function of the system, frequency resolution of the  
35 Fourier transform, type of the window function, and typical frequency of the waveform data.  
36 Compared with conventional calibration methods, the proposed method provides more accurate  
37 results in various cases. This method is useful for calibration of general radio wave signals  
38 through passed LTI systems as well as for calibration of plasma waves observed in space.

39

## 40 **1 Introduction**

41 Time-sequential signals are measured and analyzed for multi purposes in various  
42 scientific fields. The following are some typical examples of time-sequential signals: brain  
43 waves and electrocardiograms in medical science, acoustic signals and alternating current signals  
44 in engineering science, electromagnetic waves in physics, and seismic waves in geoscience.  
45 Particularly, in space exploration, many satellites have observed various types of electric and  
46 magnetic field waveforms to investigate and develop space plasma physics (e.g., Angelopoulos,  
47 2008; Mauk et al., 2013; Burch et al., 2016; Miyoshi et al., 2018). Most of the signals are  
48 essentially continuous analog signals and include unexpected noises, such as rapid fluctuations  
49 and/or tardily varying offsets. To observe the signals quantitatively and convert them into  
50 discrete digital data, the signals should be detected by sensors, amplified using amplifiers, and  
51 passed through filters to eliminate noises. The sensors, amplifiers, filters, and other processor  
52 types, expressed as linear time-invariant (LTI) systems, serve expected functions; however, they  
53 also provide unintentional signal modification, such as gain changes and phase shifts. Removing  
54 the unintentional modification from output signals is called calibration, and the output signals are  
55 divided by the transfer function of the systems in the frequency domain, which is a conventional  
56 calibration method (Matsuda et al., 2021). Because time-sequential signals that should be  
57 calibrated typically comprise finite data points, the conventional calibration method is effective  
58 only when the number of data points is sufficiently large and the sampling frequency is much  
59 shorter than the typical frequencies of the observed signals. In some cases, however, the number  
60 of data points of the observed signals and/or the calculation resource should be limited, and  
61 dividing the signals by the transfer function alone is not sufficient for the calibration. For  
62 example, the Software-type Wave-Particle Interaction Analyzer (S-WPIA) (Kato et al., 2018)  
63 aboard the Arase satellite (Miyoshi et al., 2018) requires onboard calibration processes for  
64 electromagnetic waveform data, and the calculation resources for each time window are limited  
65 to several hundred points (Hikishima et al., 2014; 2018).

66 In this paper, we focus on cases with short data sizes, such as a case where the short-time  
 67 Fourier transform (STFT) algorithm is used, and we propose a novel calibration method for  
 68 analog filters that have a non-negligible group delay. The methodology and principles are  
 69 described in Section 2. The method for quantifying the accuracy of the calibration methods is  
 70 presented in Section 3, and the example calibration result is presented in Section 4. Next, we  
 71 discuss the relationship between the calculation time and resources, and the characteristics of  
 72 each calibration method in Section 5.

## 73 2 Principle and Methodology

### 74 2.1 Main principle

75 Based on signal processing textbooks (e.g., Bendat & Piersol, 2010), the calibration  
 76 process is expressed using the Fourier transform. Let  $x_{\text{in}}$  and  $x_{\text{out}}$  be input and output signals  
 77 as functions of time  $t$ . The modification caused by a system is expressed by the convolution of a  
 78 response of the system to an impulse  $g(t)$  such as

$$79 \quad x_{\text{out}}(t) = g(t) * x_{\text{in}}(t). \quad (1)$$

80 Let  $\mathcal{F}$  and  $\mathcal{F}^{-1}$  be the operations of the Fourier transform (FT) and the inverse Fourier  
 81 transform (IFT) for a function, respectively; let  $X(\omega)$  and  $G(\omega)$  be  $X(\omega) = \mathcal{F}[x(t)]$  and  
 82  $G(\omega) = \mathcal{F}[g(t)]$ , where  $\omega$  is the angular frequency of the signals. Here,  $G(\omega)$  represents the  
 83 transfer function of the system. Because the convolution operation in the time domain is  
 84 equivalent to multiplying a window in the frequency domain, equation (1) can be rewritten as

$$85 \quad X_{\text{out}}(\omega) = G(\omega) \cdot X_{\text{in}}(\omega). \quad (2)$$

86 By introducing  $\mathcal{C}$  operator as a sequence of operations that perform the FT of signals, dividing  
 87 the signals  $G(\omega)$  in the frequency domain, and then performing the IFT, such as

$$88 \quad \mathcal{C}[f(x)] = \mathcal{F}^{-1} \left[ \frac{\mathcal{F}\{x(t)\}}{G(\omega)} \right] = \mathcal{F}^{-1} \left[ \frac{X(\omega)}{G(\omega)} \right], \quad (3)$$

89 the input signal  $x_{\text{in}}(t)$  can be ideally reproduced by the following process:

$$90 \quad x_{\text{in}}(t) = \mathcal{F}^{-1} \left[ \frac{\mathcal{F}[x_{\text{out}}(t)]}{G(\omega)} \right] = \mathcal{C}[x_{\text{out}}(t)]. \quad (4)$$

91 In actual cases, the discrete Fourier transform (DFT) and the inverse discrete Fourier transform  
 92 (IDFT) are commonly used in place of  $\mathcal{F}$  and  $\mathcal{F}^{-1}$  in equation (4) owing to the limited number  
 93 of data points. Let  $t_n$ ,  $f_s$ ,  $N$ , and  $T$  be the detected time, the sampling frequency of the  
 94 detected data, the number of data points, and the time duration of the data (the window size of  
 95 the data), and let  $k$ ,  $m$ , and  $n$  be index integers. Thus, DFT and IDFT are defined as

$$96 \quad X(\omega_m) = \mathcal{F}_D[x(t_n)] = \frac{1}{N} \sum_{n=0}^{N-1} x(t_n) e^{-i\omega_k t_n} = \frac{1}{N} \sum_{n=0}^{N-1} x(t_n) e^{-\frac{2\pi i m n}{N}}, \quad (5)$$

$$97 \quad x(t_n) = \mathcal{F}_D^{-1}[X(\omega_m)] = \sum_{k=0}^{N-1} X(\omega_m) e^{i\omega_k t_n} = \sum_{k=0}^{N-1} x(\omega_m) e^{\frac{2\pi i m n}{N}}, \quad (6)$$

98 where  $t_n = n\Delta t$ ,  $\omega_m = m\Delta\omega = 2\pi m\Delta f$ ,  $\Delta t = \frac{1}{f_s} = \frac{T}{N}$ ,  $\Delta f = \frac{f_s}{N}$ . We define the operation  $\mathcal{C}_D$  as  
 99 the calibration method in (4) applied to discrete finite data with the DFT/IDFT expressed as

$$100 \quad \mathcal{C}_D[x_{\text{out}}(t_n)] = \mathcal{F}_D^{-1} \left[ \frac{\mathcal{F}_D[x_{\text{out}}(t_n)]}{G(\omega_m)} \right], \quad (7)$$

101 where  $\mathcal{C}_D$  is the  $\mathcal{C}$  operation using the DFT/IDFT for digital data. Note that, for the case where  
 102 the frequency resolution  $\Delta\omega$  (or  $\Delta f$ ) is small, that is, the number of data points  $N$  is large, the  
 103 calibration method described in (4) is reasonable for the estimation of input data with high  
 104 accuracy. However,  $x_{\text{in}} \neq \mathcal{C}[x_{\text{out}}]$  for finite  $N$ .

105 In typical DFT/IDFT processes, which include the STFT process, the data to be applied  
 106 to the DFT/IDFT are multiplied by a window function to taper off to the edges and avoid side-  
 107 lobe effects owing to discontinuity at the edges. Here, let  $w(t_n)$  be a window function in the  
 108 time domain. By applying the operation  $\mathcal{C}_D$  to the tapered output data, we can estimate the input  
 109 data using the following operation  $\mathcal{C}_w$ :

$$110 \quad \mathcal{C}_w[x_{\text{out}}(t_n), w(t_n)] = \frac{\mathcal{C}_D[w(t_n) \cdot x_{\text{out}}(t_n)]}{w(t_n)} = \frac{\mathcal{F}^{-1} \left[ \frac{\mathcal{F}[w(t_n) \cdot x_{\text{out}}(t_n)]}{G(\omega_m)} \right]}{w(t_n)}. \quad (8)$$

111 The calibration process expressed by operation  $\mathcal{C}_w$  is more accurate than  $\mathcal{C}_D$  for a sufficiently  
 112 large  $N$  because the side lobes become small in the frequency domain by edge tapering.  
 113 However, the operation  $\mathcal{C}_w$  cannot exactly reproduce the input data  $x_{\text{in}}$ . Let  $W$  be the spectrum  
 114 of the window function in the frequency domain, expressed as  $W(\omega) = \mathcal{F}[w(t)]$ . The relation  
 115 between the transfer function and tapered data in the time domain can be expressed as

$$116 \quad w(t) \cdot x_{\text{out}}(t) = w(t) \cdot (g(t) * x_{\text{out}}(t)), \quad (9)$$

117 and its relation in the frequency domain is easily derived from equation (9) as

$$118 \quad W(\omega) * X_{\text{out}}(\omega) = W(\omega) * (G(\omega) \cdot X_{\text{in}}(\omega)). \quad (10)$$

119 Based on equations (9) and (10), because the windowing and filtering processes are conjugate  
 120 operations of each other, the convoluted window function in the frequency domain is also  
 121 modified by the calibration process divided by the transfer function  $G$  in the frequency domain.  
 122 This fact is also expressed as  $x_{\text{in}} \neq \mathcal{C}_w[x_{\text{out}}]$  for finite  $N$  owing to  $(W * (G \cdot X_{\text{in}}))/G \neq W * X_{\text{in}}$ .  
 123

124

## 125 2.2 Modulation of window functions

126 In this section, to evaluate the difference between  $x_{\text{in}}$  and  $\mathcal{C}_w[x_{\text{out}}]$ , we quantify the  
 127 unintentional modulation of window functions in the calibration process. First, we assume a  
 128 simple case in which the output signals are expressed as a monotonic sinusoidal wave as

$$129 \quad x_{\text{out}}(t_n) = A_0 e^{i(\omega_0 t_n + \phi_0)}, \quad (11)$$

130 where  $A_0$ ,  $\phi_0$ , and  $\omega_0$  are the amplitude, initial phase, and frequency of the waveform,  
 131 respectively. The wave period of the signals is assumed as an integer multiple of the time width  
 132 of the window ( $\omega_0 = m_0 \Delta\omega$  with  $m_0 \in \mathbb{N}$ ). Note that because  $\Delta\omega$  is defined as  $\Delta\omega = 2\pi/T$ ,  
 133  $\Delta\omega$  represents not only the frequency resolution of the DFT/IDFT but also the fundamental  
 134 frequency of the window function. In this case, by applying the DFT/IDFT described in (5) and  
 135 (6), the frequency spectra of the output signals are succinctly expressed as

$$136 \quad X_{\text{out}}(\omega_m) = A_0 e^{i\phi_0} \delta_{m,m_0}, \quad (12)$$

137 where  $\delta_{i,j}$  is the Kronecker delta. Let  $|G(\omega)|$  and  $\theta(\omega)$  be the magnitude and argument of the  
 138 complex transfer function  $G(\omega)$  as written by  $|G(\omega)| = \text{abs}(G(\omega)) =$   
 139  $\sqrt{\text{Re}[G(\omega)] + \text{Im}[G(\omega)]}$  and  $\theta(\omega) = \arg(G(\omega)) = \tan^{-1}(\text{Im}[G(\omega)]/\text{Re}[G(\omega)])$ , where  
 140  $\text{Re}[z]$  and  $\text{Im}[z]$  are the real and imaginary parts of a complex number  $z$ , respectively. The  
 141 operation  $\mathcal{C}_D$  for the output signal without any window function can be rewritten as

$$142 \quad \mathcal{C}_D[x_{\text{out}}(t_n)] = \mathcal{F}_D^{-1} \left[ \frac{A_0 e^{i(\phi_0 - \theta(\omega_0))}}{|G(\omega_0)|} \delta_{m,m_0} \right] = \frac{A_0}{|G(\omega_0)|} e^{i(\omega_0 t_n + \phi_0 - \theta(\omega_0))}. \quad (13)$$

143 For general cases, the output signals  $x_{\text{out}}(t_n)$  can be expanded by a series of exponential  
 144 functions using DFT:

$$145 \quad x_{\text{out}}(t_n) = \sum_{m=0}^{N-1} X_m e^{i\omega_m t_n}, \quad (14)$$

146 where  $X_m = X(\omega_m) = \mathcal{F}_D[w(t_n)]$ . The window function  $w(t_n)$  can also be expanded as

$$147 \quad w(t_n) = \sum_{k=0}^{N-1} W_k e^{ik\Delta\omega t_n}, \quad (15)$$

148 where  $W_k = W(\omega_k) = \mathcal{F}_D[w(t_n)]$ .

149 Assuming the condition of

$$150 \quad \frac{W_N}{2} \ll W_0, \quad (16)$$

151 the following approximation can be derived from equation (15),

$$152 \quad w(t_n) \simeq W_0 + \sum_{k=1}^{\frac{N}{2}-1} \{W_k e^{ik\Delta\omega t_n} + W_{-k} e^{-ik\Delta\omega t_n}\}. \quad (17)$$

153 The right- and left-hand sides of approximation (17) should be exactly equivalent because  $W_{\frac{N}{2}} =$   
 154 0 in the case of the window function expressed as a simple summation of the cosine function  
 155 (e.g., the Hamming window, etc.). By multiplying both sides of equations (14) by (17), we obtain  
 156 the following expression:

$$157 \quad w(t_n) \cdot x_{\text{out}}(t_n) \simeq \sum_{m=0}^{N-1} X_m \left\{ W_0 e^{i\omega_m t_n} + \sum_{k=1}^{\frac{N}{2}-1} \{W_k e^{i(\omega_m+k\Delta\omega)t_n} + W_{-k} e^{i(\omega_m-k\Delta\omega)t_n}\} \right\}. \quad (18)$$

158 The first term on the right-hand side of equation (18) mainly indicates a peak point of the main  
 159 lobe of signals (including side lobes), and the other terms corresponding to the accumulation of  
 160  $k$  mainly indicate the main lobe expansion around the signal frequencies ( $\sim \omega_m \pm k\Delta\omega$ )  
 161 (including side-lobe reduction parts). Here, we introduce the new parameters  $W_{k,m}^+$ ,  $W_{k,m}^-$ ,  $\theta_{k,m}^+$ ,  
 162 and  $\theta_{k,m}^-$  with double sign in the same order as

$$163 \quad W_{k,m}^{\pm} = \frac{|G(\omega_m)|}{|G(\omega_m \pm k\Delta\omega)|} W_{\pm k}, \quad (19)$$

$$164 \quad \theta_{k,m}^{\pm} = \frac{\theta(\omega_m + k\Delta\omega) \pm \theta(\omega_m - k\Delta\omega)}{2}. \quad (20)$$

165 Using these parameters expressed as (19) and (20) and applying the description of  
 166 operation  $\mathcal{C}_D$  expressed as (13) to equation (18), the following expressions can be derived:

$$167 \quad \mathcal{C}_D[w(t_n) \cdot x_{\text{out}}(t_n)]$$

$$168 \quad \simeq \sum_{m=0}^{N-1} X_m \left[ \frac{W_0}{|G(\omega_m)|} e^{i(\omega_m t_n - \theta(\omega_m))} \right.$$

$$169 \quad \left. + \sum_{k=1}^{\frac{N}{2}-1} \left[ \frac{W_k e^{i((\omega_m+k\Delta\omega)t_n - \theta(\omega_m+k\Delta\omega))}}{|G(\omega_m + k\Delta\omega)|} + \frac{W_{-k} e^{i((\omega_m-k\Delta\omega)t_n - \theta(\omega_m-k\Delta\omega))}}{|G(\omega_m - k\Delta\omega)|} \right] \right]$$

$$170 \quad = \sum_{m=0}^{N-1} \frac{X_m}{|G(\omega_m)|} \left\{ W_0 e^{i(\omega_m t_n - \theta(\omega_m))} \right.$$

$$171 \quad \left. + \sum_{k=1}^{\frac{N}{2}-1} \left[ W_{k,m}^+ e^{i((\omega_m+k\Delta\omega)t_n - (\theta_{k,m}^+ + \theta_{k,m}^-))} + W_{k,m}^- e^{i((\omega_m-k\Delta\omega)t_n - (\theta_{k,m}^+ - \theta_{k,m}^-))} \right] \right\}. \quad (21)$$

172 If we assume

$$173 \quad \theta(\omega_m) \simeq \theta_{k,m}^+, \quad (22)$$

174 the condition (22) is equivalent to

$$175 \quad \frac{1}{2}(k\Delta\omega)^2 \ll \frac{|\theta(\omega_m)|}{|\theta''(\omega_m)|} \quad (\text{for all } k) \quad (23)$$

176 because  $\theta_{k,m}^+$  can be approximated using Taylor series expansion as

$$177 \quad \theta_{k,m}^+ = \frac{\theta(\omega_m + k\Delta\omega) + \theta(\omega_m - k\Delta\omega)}{2} = \theta(\omega_m) + \frac{1}{2}(k\Delta\omega)^2\theta''(\omega_m) + \dots \quad (24)$$

178 Under the condition of inequality (23), equation (21) can be rewritten as

$$179 \quad \mathcal{C}_D[w(t_n) \cdot x_{\text{out}}(t_n)] \simeq \sum_{m=0}^{N-1} \left\{ w_{\text{sh}}(t_n, \omega_m) \left( \frac{X_m}{|G(\omega_m)|} e^{i(\omega_m t_n - \theta(\omega_m))} \right) \right\}, \quad (25)$$

180 where

$$181 \quad w_{\text{sh}}(t_n, \omega_m) = W_0 + \sum_{k=1}^{\frac{N}{2}-1} \left\{ W_{k,m}^+ e^{i(k\Delta\omega t_n - \theta_{k,m}^-)} + W_{k,m}^- e^{-i(k\Delta\omega t_n - \theta_{k,m}^-)} \right\}. \quad (26)$$

182 Introducing  $\tilde{W}_{k,m}^+$  and  $\tilde{W}_{k,m}^-$ , respectively as

$$183 \quad \tilde{W}_{k,m}^\pm = W_{k,m}^+ \pm W_{k,m}^-, \quad (27)$$

184 the expression (26) can be rewritten as

$$185 \quad w_{\text{sh}}(t_n, \omega_m) = W_0 + \sum_{k=1}^{\frac{N}{2}-1} \left\{ \tilde{W}_{k,m}^+ \cos(k\Delta\omega t_n - \theta_{k,m}^-) + i\tilde{W}_{k,m}^- \sin(k\Delta\omega t_n - \theta_{k,m}^-) \right\}. \quad (28)$$

186 Consequently, we can derive  $x_{\text{in}}(t_n) \neq \mathcal{C}_w[x_{\text{out}}(t_n)] = \mathcal{C}_D[w(t_n) \cdot x_{\text{out}}(t_n)]/w(t_n)$  because of  
 187  $w(t_n) \neq w_{\text{sh}}(t_n, \omega_m)$  in (25). This unexpected discordance is mainly caused by the main lobe  
 188 expansion shown in (18). The main lobe expansion terms are unintentionally divided by the  
 189 transfer function at expanded frequencies ( $\sim \omega_m \pm k\Delta\omega$ ), described as the second and third  
 190 terms of equation (21), and it yields the unexpected modulation of the window function.

191 Equation (28) shows that the amplitude of the window function is rotated and/or extended by  
 192  $\tilde{W}_{k,m}^+$  and  $\tilde{W}_{k,m}^-$  in the complex space, and the phase of the window function is shifted by  $\theta_{k,m}^-$ ,  
 193 which is the local linearity of the phase transfer function in the time domain. Because the  
 194 approximations are established based on the assumptions expressed as inequalities (16) and (23),  
 195 the approximations are reasonable when the following three conditions are satisfied:

- 196 • Condition A (for the window function): A sufficiently small  $K$ , which is defined as the  
 197 maximum  $k$  satisfying  $W_k \neq 0$ , is required. That is, the window function should  
 198 comprise low-order cosine functions. This condition also indicates that approximation  
 199 (23) is not effective for the case of window functions that include high  $k$  components  
 200 (e.g., the Gaussian window, the triangle window, the sine window (the half-cosine  
 201 window), etc.)
- 202 • Condition B (for frequency resolution): A sufficiently small  $\Delta\omega$  is required. That is, the  
 203 sampling frequency  $f_s$  should be sufficiently high, and/or the data length  $N$  (or  $T$ )  
 204 should be sufficiently large.
- 205 • Condition C (for the transfer function): A roughly small  $\theta''$  is required. That is, the  
 206 transfer function of the system should be locally linear in the range of  $\pm k\Delta\omega$ . Note that  
 207 the transfer function does not have a completely linear phase response in the frequency  
 208 domain.

209 In extremely small  $\Delta\omega$  cases (or large  $N$ ), the factor  $w_{\text{sh}}(t_n, \omega_m)$  in the approximation (25)  
 210 expressed as equation (26), which corresponds to the unintentionally modulated window  
 211 function, are almost equal to the  $w(t_n)$  expressed as equation (17) because  $W_{k,m}^{\pm}$  and  $\theta_{k,m}^-$  are  
 212 approximately equal to  $W_{\pm k}$  and 0, respectively. Therefore, the discordance between  
 213  $\mathcal{C}_w[x_{\text{out}}(t_n)]$  and  $x_{\text{in}}(t_n)$  is negligible. It should be noted that the accumulation in equation  
 214 (25) cannot be replaced with the fast Fourier transform (FFT) algorithm because the modulation  
 215 of the window function caused by operation  $\mathcal{C}_D$  occurs at each frequency in the frequency  
 216 domain.

217

### 218 2.3 Various window functions

219 In the previous section, we derived the discordance between  $\mathcal{C}_w[w(t_n) \cdot x(t_n)]$  and  
 220  $x_{\text{in}}(t_n)$ , and the discordance also depends on the type of window function. In this section, we  
 221 focus on the dependency of the modulation characteristics on the types of window functions.

222 One of the most common window functions is the cosine-sum window. The cosine-sum  
 223 window functions are represented as (e.g., Harris, 1978; Nuttall, 1981)

$$224 \quad w_{\text{cos}}(t_n) = \sum_{k=0}^K (-1)^k a_k \cos(k\Delta\omega t_n), \quad (29)$$

225 where  $K$  is the order of the cosine-sum window.  $K = 0, a_0 = 1$  corresponds to the rectangular  
 226 window with no window function,  $K = 1, a_0 = 0.5, a_1 = 0.5$  corresponds to the Hann window  
 227 (Hann, 1903; Blackman & Tukey, 1958),  $K = 1, a_0 = 0.54, a_1 = 0.46$  corresponds to the  
 228 Hamming window (Tukey & Hamming, 1949; Blackman & Tukey, 1958),  $K = 2, a_0 =$   
 229  $0.42, a_1 = 0.5, a_2 = 0.08$  corresponds to the Blackman window (Blackman & Tukey, 1958),  
 230 and  $K = 3, a_0 = 0.35875, a_1 = 0.48829, a_2 = 0.14128, a_3 = 0.01168$  corresponds to the  
 231 Blackman-Harris window (Harris, 1978). Figures 1a and 1b show these window functions in the

232 time domain and magnitude properties in the frequency domain. The black, red, yellow, green,  
 233 and blue lines correspond to the rectangular, Hamming, Hann, Blackman, and Blackman-Harris  
 234 window, respectively. It is well known that larger- $K$  cosine-sum window functions have a wider  
 235 main lobe and lower-level side lobes.

236 Tukey (1967) introduced a cosine taper window, also known as the Tukey window,  
 237 which is represented as

$$238 \quad w_{\text{Tk}}(t_n) = \begin{cases} 0.5 - 0.5 \cos \frac{\Delta\omega t_n}{T_S} & (0 < t_n < T_S) \\ 1 & (T_S \leq t_n \leq T_S + T_F) \\ 0.5 - 0.5 \cos \frac{\Delta\omega(T_w - t_n)}{T_S} & (T_S + T_F < t_n < T_w) \end{cases} \quad (30)$$

239 where  $T_S$ ,  $T_F$ , and  $T_w$  are the time length of the slope regions, the flat top region length, and the  
 240 whole window size ( $T_w = 2T_S + T_F$ ), respectively. The cases where  $T_F = 0$  and  $T_F = T_w$   
 241 correspond to the Hann window and rectangular window, respectively. Because the Tukey  
 242 window has a flat top region at the center of the window, the effect caused by the phase shift and  
 243 amplitude rotation of a window function is negligible at the flat center region, similar to the  
 244 rectangular window. Furthermore, the side-lobe effect is smaller than that of the rectangular  
 245 window because of the tapered slope regions at both edges of the window. To reduce the side-  
 246 lobe effects more than that of the Tukey window, including the merit of the rectangular window,  
 247 we define the ‘‘Tukey-type’’ windows by combining the Tukey window and the cosine-sum  
 248 windows as

$$249 \quad w_{\text{Tc}}(t) = \begin{cases} \sum_{k=0}^N (-1)^k a_k \cos\left(\frac{k\Delta\omega t_n}{T_S}\right) & (0 < t_n < T_S) \\ 1 & (T_S \leq t_n \leq T_S + T_F) \\ \sum_{k=0}^N (-1)^k a_k \cos\left(\frac{k\Delta\omega(T_w - t_n)}{T_S}\right) & (T_S + T_F < t_n < T_w) \end{cases} \quad (31)$$

250 For example, if we choose the Hamming window as a tapering curve, we can define the Tukey-  
 251 Hamming window as

$$252 \quad w_{\text{TH}}(t) = \begin{cases} 0.54 - 0.46 \cos \frac{\Delta\omega t_n}{T_S} & (0 < t_n < T_S) \\ 1 & (T_S \leq t_n \leq T_S + T_F) \\ 0.54 - 0.46 \cos \frac{\Delta\omega(T_w - t_n)}{T_S} & (T_S + T_F < t_n < T_w) \end{cases} \quad (32)$$

253 Figures 1c and 1d show the time and frequency properties of four types of Tukey-type window  
 254 functions and a rectangular window function with the same length of the flat region ( $r =$   
 255  $T_F/T_w = 0.3$ ). The black, red, yellow, green, and blue lines correspond to the rectangular,  
 256 Tukey-Hamming, Tukey-Hann, Tukey-Blackman, and Tukey-Blackman-Harris window,

257 respectively. Because the phase shift effect described in the previous section results from the  
 258 expanded main lobe, the Tukey-Hamming window should be one of the most useful windows in  
 259 the displayed Tukey-type windows in Figures 1c and 1d. Figures 1e and 1f show the time and  
 260 frequency properties of the Tukey-Hamming windows for different lengths of the flat region.  
 261 The red, yellow, green, cyan, blue, and black lines correspond to  $r = 0, 0.2, 0.4, 0.6, 0.8,$  and  $1,$   
 262 respectively. Note that  $r = 0$  and  $1$  correspond to the normal Hamming window and the  
 263 rectangular window, respectively. The longer flat region makes higher side lobes around the  
 264 main lobe like the rectangular window; therefore, the parameter roughly within  $0.2 < r < 0.6$   
 265 seems useful for the calibration process.

266 Based on the above discussion and the description, two types of processes are  
 267 conceivable as accurate waveform calibration with a window function: (1) Use a Tukey-type  
 268 (particularly, Tukey-Hamming) window function to reduce side lobes, and (2) use a low-order  
 269 cosine-sum window function and estimate the modification of a window function at each  
 270 frequency. The latter method is presented in the previous section, and here, we describe a method  
 271 specific to the first-order cosine-sine sum window functions.

272 In the case of the first-order cosine-sine sum window function (e.g., Hann window,  
 273 Hamming window, etc.), the window function is expressed as

$$274 \quad w_1(t_n) = a_0 - a_1 \cos(\Delta\omega t_n), \quad (33)$$

$$275 \quad w_1(t_n) = a_0 - \frac{a_1}{2} e^{i\Delta\omega t_n} - \frac{a_1}{2} e^{-i\Delta\omega t_n}, \quad (34)$$

276 and substituting (34) and (27) in (19) and (20), respectively, we can replace the following  
 277 expression:

$$278 \quad \tilde{W}^\pm(\omega) = -\frac{a_1}{2} \left\{ \frac{|G(\omega)|}{|G(\omega + \Delta\omega)|} \pm \frac{|G(\omega)|}{|G(\omega - \Delta\omega)|} \right\}, \quad (35)$$

$$279 \quad \theta^\pm(\omega) = \frac{\theta(\omega + \Delta\omega) \pm \theta(\omega - \Delta\omega)}{2}. \quad (36)$$

280 Using (35) and (36), the modulated window function (28) is rewritten as

$$281 \quad w_{\text{sh1}}(t_n, \omega_m) = a_0 + \tilde{W}_m^+ \cos(\Delta\omega t_n - \theta_m^-) + i\tilde{W}_m^- \sin(\Delta\omega t_n - \theta_m^-). \quad (37)$$

282 where  $\tilde{W}_m^\pm = \tilde{W}^\pm(\omega_m)$ , and  $\theta_m^- = \theta^-(\omega_m)$ . Based on the above, we propose a novel method to  
 283 calibrate the waveform accurately with the first-order cosine-sine sum window function, written  
 284 as

$$285 \quad x_{\text{in}}(t_n) \simeq \sum_{m=0}^{N-1} \frac{1}{w_{\text{sh1}}(t_n, \omega_m)} \cdot \frac{\mathcal{F}_D[w_1(t_n) \cdot x_{\text{out}}(t_n)] e^{i(\omega_m t_n - \theta(\omega_m))}}{|G(\omega_m)|}. \quad (38)$$

286 Note that the first-order cosine-sum window functions automatically satisfy condition A  
 287 described in the previous section; however, conditions B and C are still required for the

288 approximation. Under these conditions, we can use any type of window function such as a high-  
 289 order cosine-sum window function by substituting  $W_{\pm k}$  into  $(-1)^k a_k/2$  and replacing  
 290  $w_{sh1}(t_n, \omega_m)$  by  $w_{sh}(t_n, \omega_m)$  in equation (28).

291

## 292 **2.4 List of calibration methods**

293 Figure 2 summarizes the flowcharts of the conceivable calibration procedures for the  
 294 STFT cases. The details of the methods are as follows:

### 295 **2.4.1 Method 1**

296 Method 1 processes are shown with yellow arrows in Figure 2. The split data for STFT  
 297 are not multiplied by any window function (or multiplied by a rectangular window as a window  
 298 function), the data are calibrated in the frequency domain, and the calibrated short-time data are  
 299 connected in the time domain. The sequence of these processes, except for splitting and merging,  
 300 can be described as the operation  $\mathcal{C}al_1$  expressed as

$$301 \quad \mathcal{C}al_1[x_{out}(t_n)] = \mathcal{C}_D[x_{out}(t_n)] = \mathcal{F}_D^{-1} \left[ \frac{\mathcal{F}_D[x_{out}(t_n)]}{G(\omega_m)} \right]. \quad (39)$$

302 In the case where the typical wave period of the signals comprises integer multiples of  
 303 the time width of the STFT time window or in the case where the number of data points in the  
 304 STFT time window is sufficiently large, the calibrated signals are ideally identical to the input  
 305 signals. Conversely, when the typical wave period of the signals is not expressed by integers or  
 306 half-integer multiples of the time width of the window, the calibrated signals significantly  
 307 disagree with the input signals owing to side-lobe effects in the DFT process.

### 308 **2.4.2 Method 2**

309 Method 2 processes are shown with green arrows in Figure 2. Split data for STFT are  
 310 multiplied by a cosine-sum window in the time domain and calibrated in the frequency domain.  
 311 The calibrated short-time data inverse-transformed into waveforms in the time domain are  
 312 divided by the window function, and subsequently the data are connected in the time domain. A  
 313 sequence of the processes, except for splitting and merging, can be described as the operation  
 314  $\mathcal{C}al_2$  expressed as

$$315 \quad \mathcal{C}al_2[x_{out}(t_n)] = \mathcal{C}_w[x_{out}(t_n), w(t_n)] = \frac{\mathcal{F}^{-1} \left[ \frac{\mathcal{F}[w(t_n) \cdot x_{out}(t_n)]}{G(\omega_m)} \right]}{w(t_n)}. \quad (40)$$

316 In this study, the Hamming window was used as  $w(t_n)$  in the Method 2 process.

317 The side-lobe effects can be drastically reduced by the window function compared to the  
 318 data calibrated by Method 1; however, the main lobe expansion effect is not negligible except for  
 319 the case of sufficiently large data points.

### 320 2.4.3 Method 3

321 Method 3 processes are shown with blue arrows in Figure 2. Split data for STFT are  
 322 multiplied by a Tukey-type window function (especially, a Tukey-Hamming window is useful)  
 323 in the time domain and calibrated in the frequency domain. The calibrated short-time data  
 324 inverse-transformed into waveforms in the time domain are divided by the window function;  
 325 subsequently, the calibrated data are connected in the time domain. A sequence of the processes,  
 326 except for splitting and merging, can be described as operation  $\mathcal{C}al_3$  expressed as

$$327 \quad \mathcal{C}al_3[x_{\text{out}}(t_n)] = \mathcal{C}_w[x_{\text{out}}(t_n), w_{\text{TH}}(t_n)] = \frac{\mathcal{F}^{-1} \left[ \frac{\mathcal{F}[w_{\text{TH}}(t_n) \cdot x_{\text{out}}(t_n)]}{G(\omega_m)} \right]}{w_{\text{TH}}(t_n)}, \quad (41)$$

328 where  $w_{\text{TH}}$  is the Tukey-Hamming window, described in (32). The difference between Method  
 329 2 and Method 3 is only a window function used in the processes.

330 The side-lobe effects can be roughly reduced by the tapering sections of the Tukey-type  
 331 window function compared to the data calibrated by Method 1, and the main lobe expansion  
 332 effect is also reduced by the flat section of the Tukey-type window function compared to the data  
 333 calibrated using Method 2.

### 334 2.4.4 Method 4 (a novel method)

335 Method 4 is a novel proposed method, shown with a red line flow in Figure 2. Split data  
 336 for STFT are multiplied by a cosine-sum window in the time domain, and the transformed data  
 337 are calibrated in the frequency domain, as in Method 2. The calibrated spectral data are inverse-  
 338 transformed into waveforms in the time domain at each frequency, and in parallel, the modulated  
 339 window functions are estimated at each frequency using (28) or (37). The calibrated waveforms  
 340 at each frequency are divided by the estimated window functions at each frequency, respectively,  
 341 and accumulated over all frequencies. The accumulated waveforms are connected in the time  
 342 domain. A sequence of the processes except for splitting and merging can be described as  
 343 operation  $\mathcal{C}al_4$  expressed as

$$344 \quad \mathcal{C}al_4[x_{\text{out}}(t_n)] = \sum_{m=0}^{N-1} \frac{1}{w_{\text{sh}}(t_n, \omega_m)} \cdot \frac{\mathcal{F}_D[w(t_n) \cdot x_{\text{out}}(t_n)] e^{i(\omega_m t_n - \theta(\omega_m))}}{|G(\omega_m)|}, \quad (42)$$

345 where  $w$  and  $w_{\text{sh}}$  are the applied and estimated window functions, respectively, and  $w_{\text{sh}}$  is  
 346 calculated using (28) and (37). In this study, the Hamming window is used for  $w$  such as  $w_1$   
 347 shown in (33), and  $w_{\text{sh}}$  is calculated by  $w_{\text{sh}1}$ , which is described in (35), (36), and (37).

348 The side-lobe effects are significantly reduced by the window function, similar to the data  
 349 calibrated by Method 2, and the main lobe expansion effect is also drastically eliminated by the  
 350 estimation of the modulation of the window function. However, we cannot apply the FFT for the  
 351 IDFT process, and we should perform the accumulation in (42) manually. The accumulation can  
 352 also be interpreted as a manual deconvolution in the time domain. Therefore, the calculation time  
 353 is much longer (it takes about  $\mathcal{O}(N^2)$ ) than that of the other methods (corresponding to

354  $\mathcal{O}(\frac{1}{2}N \log_2 N)$ .

355

### 356 **3 Evaluation Method**

357 To evaluate our proposed method (Method 4) and the other three calibration methods  
 358 described in Section 2.4.4., we perform the test calibration using low-pass filters and sinusoidal  
 359 waveform data as the processing system and signals, respectively.

360

#### 361 **3.1 Low-pass filters**

362 We evaluated the calibration methods using three types of analog low-pass filters as the  
 363 processing system: a first-order RC filter, a Butterworth filter, and a Bessel filter. The transfer  
 364 function of the first-order RC filter (RC1) is the simplest low-pass filter and is expressed as

$$365 \quad G_{\text{RC1}}(f) = \frac{G_0}{1 + \frac{f}{f_{\text{cutoff}}}i}. \quad (43)$$

366 Here,  $f_{\text{cutoff}}$  and  $G_0$  are the cutoff frequency and offset value corresponding to the DC gain,  
 367 respectively.

368 A Butterworth filter (Butterworth, 1930) is designed as a filter with a maximally steep cutoff  
 369 property. The transfer function of the  $l$ -th order Butterworth filter is expressed as

$$370 \quad G_{\text{BW}l}(f) = \frac{G_0}{P_l^{\text{BW}}\left(\frac{f}{f_{\text{cutoff}}}i\right)}. \quad (44)$$

371 Here,  $P_l^{\text{BW}}(s)$  is the  $l$ -th degree Butterworth polynomial for complex variable  $s$  expressed as

$$372 \quad P_l^{\text{BW}}(s) = \begin{cases} \prod_{k=1}^{\frac{l}{2}} \left[ s^2 - 2s \cos\left(\frac{2k+l-1}{2l}\pi\right) + 1 \right] & \text{for even } n, \\ (1+s) \prod_{k=1}^{\frac{l-1}{2}} \left[ s^2 - 2s \cos\left(\frac{2k+l-1}{2l}\pi\right) + 1 \right] & \text{for odd } n. \end{cases} \quad (45)$$

373 A Bessel filter (Kiyasu, 1943; Thomson, 1949) was designed as a filter with a maximally linear  
 374 phase response. The transfer function of the  $l$ -th order Bessel filter is expressed as

$$G_{BSl}(f) = \frac{G_0 P_l^{BS}(0)}{P_l^{BS}\left(\frac{f}{f_{\text{cutoff}}}\right)}. \quad (46)$$

Here,  $P_l^{BS}(s)$  is the  $l$ -th degree reverse Bessel polynomial represented as

$$P_l^{BS}(s) = \sum_{k=0}^l \frac{(2l-k)!}{2^{l-k} k! (l-k)!} s^k. \quad (47)$$

Note that both a first-order Butterworth filter and a first-order Bessel filter correspond to the first-order RC filter.

Figure 3 shows the properties of the filters with  $f_{\text{cutoff}} = 10$  kHz and  $G_0 = 1$ . (a) and (e) are the amplitude components of the transfer function  $|G(f)|$  corresponding to the gain of the filters; (b) and (f) are the phase components of the transfer function  $\theta(f)$ , and (c) and (g) are the first-order derivatives of  $\theta(f)$ , and (d) and (h) are the second-order derivatives of  $\theta(f)$ , respectively. The black, red, and blue lines correspond to the RC1, Butterworth, and Bessel filters, respectively, and the dashed and solid lines of the red and blue lines correspond to the third- and seventh-order filters, respectively. Figures 3a to 3d are plotted in the frequency range of  $10^2$  to  $10^6$  Hz with a logarithmic scale, and (e) to (h) are plotted in the frequency range of 0 to 10 kHz with a linear scale. The Butterworth filters have a flat magnitude at the passband and a steep slope at the cutoff frequency (red lines in Figure 3a) in exchange for a large phase delay at the passband (red lines in Figures 3b and 3f). The higher-order Butterworth filters provide a steeper gain cutoff and larger phase delays around the cutoff frequency. In contrast, the gain cutoff slopes of the Bessel filters are softer than those of Butterworth filters (blue lines in Figure 3a); however, the phase response is a gentle slope, such as a linear slope, and the slope does not depend on the order of the filter (blue lines in Figures 3b and 3c).  $\theta'$  shown in Figures 3c and 3g indicate phase delays and also correspond to the phase shift of a window function described as  $\theta^-$  in equations (28) and (37).

397

### 3.2 Test sinusoidal waves

The test waveform signals  $x_{\text{in}}(t_n)$  at each (arbitrary) frequency  $f_{\text{in}}$  are expressed as

$$x_{\text{in}}(t_n) = A_{\text{in}} \cos(\phi_{\text{in}}(t_n, f_{\text{in}})), \quad (48)$$

where

$$\phi_{\text{in}}(t_n, f_{\text{in}}) = 2\pi f_{\text{in}} t_n + \phi_0. \quad (49)$$

Here,  $A_{\text{in}}$  and  $\phi_0$  are the constant wave amplitude and initial phase, respectively. Note that the suffix ‘out’ represents the calibration target. The signal output from the processing system corresponds to the signals inputted into the calibration processes. The suffix ‘in’ represents data, and the signals inputted into a processing system corresponding to the signal output from the

407 calibration process. The ideal output signals are represented as

$$408 \quad x_{\text{out}}(t_n) = A_{\text{out}} \cos(\phi_{\text{out}}(t_n, f_{\text{out}})) = |G(f_{\text{in}})| A_{\text{in}} \cos(\phi_{\text{in}} + \theta(f_{\text{in}})) \quad (50)$$

409 To evaluate the accuracy of these calibration processes, we set  $x_{\text{out}}(t_n)$  as sinusoidal  
 410 waves at first, and subsequently, we compared “the correct answer” expressed as  
 411  $\frac{A_{\text{out}}}{|G(f_{\text{in}})|} \cos(\phi_{\text{out}} - \theta(f_{\text{in}}))$  and calibrated data  $\mathcal{C}al_h[x_{\text{out}}(t_n)]$  using the following indexes.

412

### 413 3.3 Evaluation parameters

414 We define three indexes: the maximum gap  $\Gamma$ , the error of amplitude  $Q$ , and the phase  
 415 difference  $D$ . First, we define  $\delta_h$  as a simple difference between the ideal signal  $x_{\text{in}}(t_n)$  and  
 416 calibrated signal  $\mathcal{C}al_h[x_{\text{out}}(t_n)]$  expressed as

$$417 \quad \delta_h(t_n) = \mathcal{C}al_h[x_{\text{out}}(t_n)] - x_{\text{in}}(t_n). \quad (51)$$

418 Note that the suffix  $h$  represents the method number corresponding to Method 1, 2, 3, or 4.  
 419 Using  $\delta_h$ , we define the maximum gap  $\Gamma$  as

$$420 \quad \Gamma_h = \max_{T_c - T_a \leq t_n \leq T_c + T_a} \left( \frac{|\delta_h(t_n) - \delta_h(t_{n-1})|}{A_{\text{in}}} \right) \times 100 [\%] \quad (52)$$

421 The maximum gap  $\Gamma$  mainly shows how seamless the joint section of the STFT data windows  
 422 is. Next, we define the error of the amplitude  $Q$ , and the phase difference  $D$  calculated by the  
 423 instantaneous amplitude and phase. The instantaneous amplitude  $\mathcal{A}_{\text{inst}}$  and the instantaneous  
 424 phase  $\mathcal{P}_{\text{inst}}$  for general  $x(t_n)$  can be respectively derived using the Hilbert transform as

$$425 \quad \mathcal{A}_{\text{inst}}[x(t_n)] = \sqrt{(x(t_n))^2 + (\mathcal{H}_D[x(t_n)])^2} \quad (53)$$

$$426 \quad \mathcal{P}_{\text{inst}}[x(t_n)] = \arg(x(t_n) + i\mathcal{H}_D[x(t_n)]) \bmod 2\pi \quad (54)$$

427 Here, the discrete Hilbert transform  $\mathcal{H}_D$  is expressed as

$$428 \quad \mathcal{H}_D[x(t_n)] = \text{Re} \left[ \mathcal{F}_D^{-1}[\tilde{X}(\omega_m)] \right] \quad (55)$$

$$429 \quad X(\omega_m) = \mathcal{F}_D[x(t_n)] \quad \text{and} \quad \tilde{X}(\omega_m) = \begin{cases} X(\omega_m) & \text{for } m = 0 \text{ and } \frac{N}{2}, \\ 2X(\omega_m) & \text{for } 0 < m < \frac{N}{2}, \\ 0 & \text{for } m > \frac{N}{2}. \end{cases} \quad (56)$$

430 By using  $\mathcal{A}_{\text{inst}}$  and  $\mathcal{P}_{\text{inst}}$ , We define the error of calibrated amplitude  $Q$  at each  $t_n$  as

$$431 \quad Q_h(t_n) = \frac{|\mathcal{A}_{\text{inst}}[\mathcal{C}al_h[x_{\text{out}}(t_n)]] - A_{\text{in}}|}{A_{\text{in}}} \times 100 [\%] \quad (57)$$

432 Because the instantaneous amplitude is not accurate around the edge of the data owing to the  
433 discontinuity effect of the DFT, we define the averaged error of the amplitude around the center  
434 area to avoid edge effects:

$$435 \quad \bar{Q}_h = \text{avg}_{T_c - T_a \leq t_n \leq T_c + T_a} (Q_h(t_n)) [\%], \quad (58)$$

436 where  $T_c$  is the center of data  $x_{\text{out}}(t_n)$  or  $x_{\text{in}}(t_n)$  expressed as  $T_c = T_{\text{total}}/2$  and  $T_a$  is the  
437 accumulation time width. In this study, we used  $T_a = T_{\text{total}}/10$ .

438 We also define the phase difference using the instantaneous phase calculated from the Hilbert  
439 transform represented as

$$440 \quad D_h(t_n) = |\mathcal{P}_{\text{inst}}[\mathcal{C}al_h[x_{\text{out}}(t_n)]] - \phi_{\text{in}}(t_n)| [\text{degree}] \quad (59)$$

441 We also define the averaged phase difference around the center area to avoid the edge effect  
442 represented as

$$443 \quad \bar{D}_h = \text{avg}_{T_c - T_a \leq t_n \leq T_c + T_a} (D_h(t_n)) [\text{degree}]. \quad (60)$$

444  $\bar{Q}$  and  $\bar{D}$  indicate the averaged accuracy of the calibration process.

445 We calculated these parameters for the five types of filters, the five combinations of  
446  $N_{\text{window}}$  and  $N_{\text{slide}}$  for sufficiently large  $N_{\text{total}}$  at each frequency in the frequency range from 0  
447 kHz to  $f_{\text{cutoff}} = 10$  kHz. Here,  $N_{\text{window}}$ ,  $N_{\text{slide}}$ , and  $N_{\text{total}}$  are the number of window widths,  
448 sliding length of the window, and total data length corresponding to  $T_{\text{total}}$  shown in Figure 4. To  
449 make the discrete Hilbert transform sufficiently accurate, we chose  $N_{\text{total}} = 10,000$  points and  
450  $f_s = 100$  kHz.

451

## 452 **4 Result and Discussion**

453 Figure 5 shows a set of sample plots of (a)  $\mathcal{C}al_h[x_{\text{out}}(t_n)]$ , (b)  $\delta_h$ , (c)  $Q_h(t_n)$ , and  
454 (d)  $D_h(t_n)$  around the center of the data. The yellow, green, blue, and red points and lines  
455 correspond to Method 1, 2, 3, and 4, respectively. To calculate this plot, we use the third-order  
456 Butterworth filter and 5.17 kHz sinusoidal waveform data with 10,000 points data corresponding  
457 to 0.1 s. The window width of the STFT and the sliding width were 128 and 64 points,  
458 respectively, and the sampling frequency was 100 kHz. The calibrated signals in Figure 5a can  
459 reproduce the input waveform; however, these results do not correspond to “the answer” exactly.  
460 Figure 5b shows the simple difference between the calibrated data and “the answer”. We can  
461 recognize a non-negligible inaccuracy in Methods 1 and 2 and discontinuities at joint sections,  
462 which exist in the center of the displayed time duration, in Methods 1, 2, and 3. Figures 5c and

463 5d show the instantaneous accuracies of the amplitude and phase, respectively. Whereas  
 464 Methods 1 and 2 include several to 10 percent errors in the calibrated amplitudes and several  
 465 degrees in the calibrated phases, the calibration errors of the amplitudes and phases in Methods 3  
 466 and 4 are smaller than those of the other methods. However, the calibration result of Method 3  
 467 still contains non-negligible errors that reach several to 10 percent and degrees around joint  
 468 sections caused by the discontinuities.

469 To reveal the general tendency, we performed the same test calibration for each  
 470 frequency, window function, and window size. Figures 6, 7, 8, and 9 show the frequency  
 471 dependences of the maximum gap  $\Gamma_h$ , the averaged error of amplitude  $\bar{Q}_h$ , and the phase  
 472 difference  $\bar{D}_h$ . Overall, Methods 1 and 2 provide less accurate calibration results, and Methods 3  
 473 and 4 provide more accurate results.

474 The plots in Figures 6 and 7 are constructed using the same window functions (the third-  
 475 order Butterworth filter) and different  $N_{\text{window}}$  and  $N_{\text{slide}}$ . Overall, the results are accurate in  
 476 the order of Methods 4, 3, 2, and 1. For the cases of  $N_{\text{window}} = 128$ , because the frequency  
 477 resolution  $\Delta f$  corresponds to 512 Hz, Method 1 provides the most accurate data at frequencies  
 478 equal to integer multiples of the frequency resolution ( $f = m_0 \Delta f$  with  $m_0 \in \mathbb{N}$ ) in the results  
 479 provided by the four methods. However, Method 1 also provides the worst accurate data at the  
 480 other frequencies, and its accuracy does not depend on the sliding number  $N_{\text{slide}}$ . Method 2  
 481 provides less accurate data, similar to Method 1. The frequency dependency of the gaps and  
 482 errors in Method 2 was roughly flat. Methods 3 and 4 provide smaller errors compared to  
 483 Methods 1 and 2, and the results from Method 3 still contain gaps. At lower frequencies that are  
 484 smaller than approximately 1.5 kHz corresponding to three waves (sequences of up and down) in  
 485 a window, the errors are larger than those at middle frequencies because side-lobe effects and a  
 486 window function modulation effect cannot be estimated with sufficient accuracy owing to a few  
 487 waves in a window. At higher frequencies, larger than approximately 8 to 9 kHz, the errors are  
 488 also larger than those at middle frequencies because the signal frequencies are closer to the  
 489 cutoff frequency and the second derivatives of the phase transfer function are larger than those at  
 490 the middle frequencies. Decreasing the slide points (such as Figures 6a, 6b, and 6c in that order)  
 491 and increasing the window width (such as Figures 7a, 7b, and 7c in that order) increases the  
 492 accuracy of the results. Increasing the window width also contributes to increasing the accuracy  
 493 of middle-frequency regions and reducing inaccurate low- and high-frequency regions.

494 Figures 8 and 9 show the dependence of the filters on the transfer function. Because the  
 495 first-order RC filter and Bessel filters shown in Figure 8 with any order have almost the same  
 496 phase properties, so-called maximally linear phase responses (black and blue lines in Figure 3),  
 497 the calculation errors caused by all methods represent almost the same properties. Comparing  
 498 Figures 9a, 9b, and 9c, the calibration results from the higher-order Butterworth filter tend to  
 499 include larger gaps and errors owing to the larger second derivatives of the phase transfer  
 500 functions (red lines in Figure 3). However, the results from Method 4 are still the most accurate  
 501 among the results of the four methods with several times of  $10^{-1}$  percent gaps and errors and  
 502 several times of  $10^{-1}$  degrees of phase errors. Summarily, Method 4 is the most accurate  
 503 calibration procedure for the four conceivable methods, and the method conspicuously exhibits  
 504 its potential for a small data point (i.e., short-time width) case and a more curved phase transfer  
 505 function case.

506 In the case of the calculation time, let  $N_{\text{split}}$  be the number of times of splitting data and  
 507 executing the FT process, and  $N_{\text{split}}$  be expressed by  $N_{\text{total}}$ ,  $N_{\text{window}}$ , and  $N_{\text{slide}}$  as  $N_{\text{split}} =$   
 508  $(N_{\text{total}} - N_{\text{window}})/N_{\text{slide}} + 1 \approx N_{\text{total}}/N_{\text{slide}}$  for  $N_{\text{total}} \gg N_{\text{window}}, N_{\text{slide}}$ . The calculation  
 509 times of the calibration process with Methods 3 and 4,  $\tau_3$  and  $\tau_4$  can be expressed as  $\tau_3 \approx$   
 510  $(N_{\text{total}} \times N_{\text{window}} \times \log_2 N_{\text{window}})/(2N_{\text{slide}})$  and  $\tau_4 \approx N_{\text{total}} \times N_{\text{window}}^2/N_{\text{slide}}$ , respectively.  
 511 For example, if we choose  $N_{\text{window}} = 2048$ ,  $N_{\text{slide}} = 2$  for Method 3, and  $N_{\text{slide}} =$   
 512  $N_{\text{window}}/2$  for Method 4, the calculation times for Methods 3 and 4 are roughly the same.  
 513 Method 4 yields a more accurate calibration; however, it requires more calculation times than  
 514 Method 3.

515 The proposed method is effective for more curved phase transfer function cases such as  
 516 the case of a filter containing a steep slope and should be applied not only to filter calibration but  
 517 also to other transfer functions that do not have linear phase characteristics (e.g., amplifier,  
 518 sensor, etc.). The qualitative tendencies of the three conventional methods and the proposed  
 519 method are summarized in Table 1. Note that each method has benefits and inexpediences, and  
 520 which method should be chosen is a matter of degree of data accuracy, depending on the  
 521 scientific/engineering purpose and practical use.

522

## 523 **5 Summary**

524 In this paper, we describe the behavior of window functions in the conventional  
 525 calibration processes of waveform data passed through LTI systems, and we propose a novel  
 526 calibration method described in Section 2.4.4. The essential process of the novel method is to  
 527 estimate the unexpected modification of a window function in the calibration process and  
 528 correcting it at each frequency in the time domain. The novel method provides sufficiently  
 529 accurate calibration results without any change in the transfer function itself, even for short-time  
 530 data cases, such as the case in which the STFT algorithm is used. We also clarified  
 531 mathematically and quantitatively why using the Tukey-type window (Method 3), which has  
 532 been used empirically, provides more accurate calibration results compared to Method 2. The  
 533 calculation time of the novel method is much longer than that of the other methods because the  
 534 FFT algorithm cannot be used in the inverse-transform process of the novel method. Which  
 535 method should be chosen is a matter of degree of data accuracy and the calculation resource  
 536 depending on the scientific/engineering purpose and practical use. As the next step of this study,  
 537 we will apply this method to electromagnetic waveform data at VLF frequency range observed  
 538 by the Plasma Wave Experiment/Waveform Capture (Kasahara et al., 2018; Matsuda et al, 2018)  
 539 aboard the Arase satellite and evaluate the accuracy and usability of our proposed method.

540

541

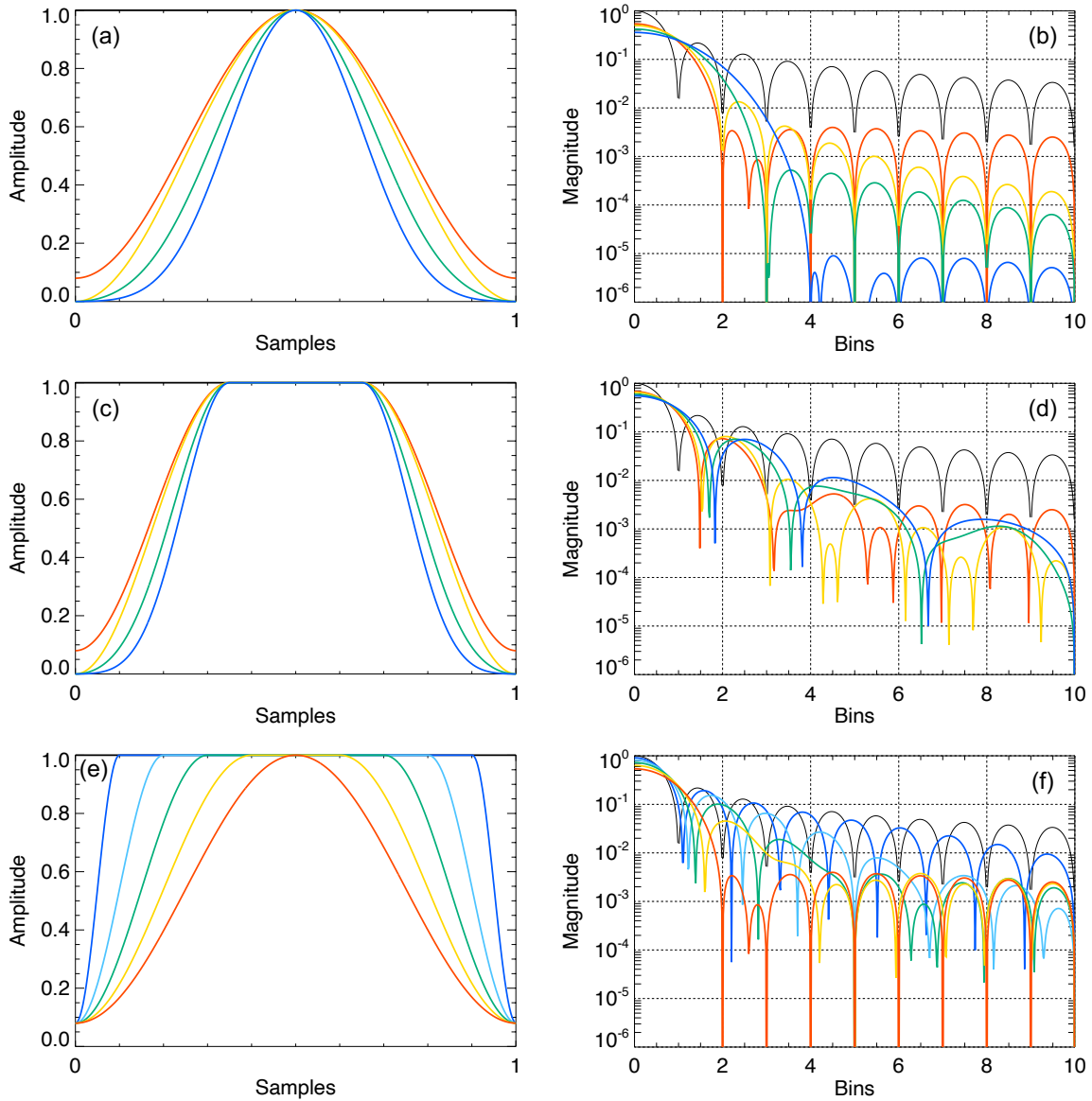
542 **Acknowledgments**

543 No datasets were used in this work, and all data in the figures can be reproduced from the  
 544 description and equations in the present study. This study was supported by Grants-in-Aid for  
 545 Scientific Research (17H00728, 18H03727, 20H01959, 20K14546, and 21K13979) of the Japan  
 546 Society for the Promotion of Science (JSPS) and JSPS-CAS bilateral project (JPJSBP10192504).  
 547 This research was also supported by the “Computational Joint Research Program (Collaborative  
 548 Research Project on Computer Science with High-Performance Computing)” at the Institute for  
 549 Space-Earth Environmental Research, Nagoya University.

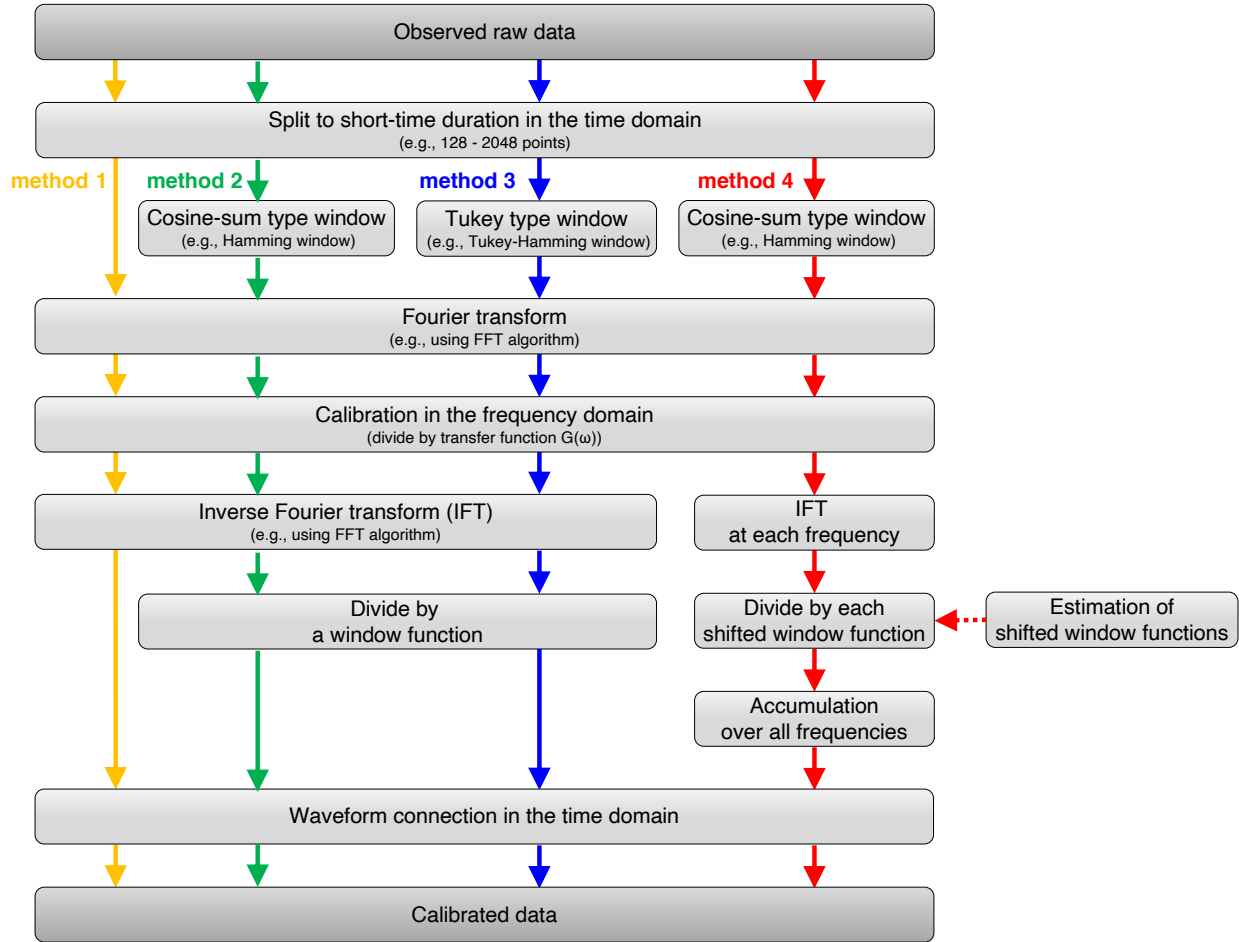
550 **References**

- 551 Angelopoulos, V. (2008), The THEMIS Mission. *Space Science Reviews*, 141, 5–34.  
 552 <https://doi.org/10.1007/s11214-008-9336-1>
- 553 Bendat, J. S., & Piersol, A. G. (2011), Random data: analysis and measurement  
 554 procedures (4th ed.). New York, NY: Wiley.
- 555 Blackman, R.B., & J. W. Tukey (1958), The measurement of power spectra: from the  
 556 point of view of communications engineering. New York, NY: Dover Publications.
- 557 Burch, J. L., Moore, T. E., Torbert, R. B., & Giles, B. L. (2013), Magnetospheric  
 558 Multiscale Overview and Science Objectives. *Space Science Reviews*, 199, 5–21.  
 559 <https://doi.org/10.1007/s11214-015-0164-9>
- 560 Butterworth, S. (1930), On the Theory of Filter Amplifiers. *Experimental Wireless and*  
 561 *the Wireless Engineer*, 7, 536–541.
- 562 Hann, J. V. (1903), *Handbook of Climatology*. London, Macmillan and Co., Ltd.
- 563 Harris, F. J. (1978), On the use of windows for harmonic analysis with the discrete  
 564 Fourier transform. *Proceedings of the IEEE*, 66(1), 51–83.  
 565 <https://doi.org/10.1109/PROC.1978.10837>
- 566 Hikishima, M., Katoh, Y., & Kojima, H. (2014), Evaluation of waveform data processing  
 567 in Wave-Particle Interaction Analyzer. *Earth Planets Space*, 66, 63.  
 568 <https://doi.org/10.1186/s40623-018-0856-y>
- 569 Hikishima, M., Kojima, H., Katoh, Y., Kasahara, Y., Kasahara, S., Mitani, T., et al.  
 570 (2018), Data processing in the Software-type wave-particle interaction analyzer on board the  
 571 Arase satellite. *Earth Planets Space*, 70, 80. <https://doi.org/10.1186/s40623-018-0856-y>
- 572 Kasahara, Y., Kasaba, Y., Kojima, H., Yagitani, S., Ishisaka, K., Kumamoto, A., et al.  
 573 (2018), The Plasma Wave Experiment (PWE) on board the Arase (ERG) satellite. *Earth, Planets*  
 574 *and Space*, 70, 86. <https://doi.org/10.1186/s40623-018-0842-4>
- 575 Katoh, Y., Kojima, H., Hikishima, M., Takashima, T., Asamura, K., Miyoshi, Y., et al.  
 576 (2018), Software-type Wave-Particle Interaction Analyzer on board the Arase satellite. *Earth*  
 577 *Planets Space* 70, 4. <https://doi.org/10.1186/s40623-017-0771-7>
- 578 Kiyasu, Z. (1943), On A Design Method of Delay Networks (the original paper is written  
 579 in Japanese). *The Journal of the Institute of Electrical Communication Engineers of Japan*,  
 580 27(8), 598–610.

- 581 Matsuda, S., Kasahara, Y., Kojima, H., Kasaba, Y., Yagitani, S., Ozaki, M., et al. (2018),  
582 Onboard software of Plasma Wave Experiment aboard Arase: instrument management and signal  
583 processing of Waveform Capture/Onboard Frequency Analyzer. *Earth, Planets and Space*, 70,  
584 75. <https://doi.org/10.1186/s40623-018-0838-0>
- 585 Matsuda, S., Kojima, H., Kasahara, Y., Kasaba, Y., Kumamoto, A., Tsuchiya, F., et al.  
586 (2021), Direct antenna impedance measurement for quantitative AC electric field measurement  
587 by Arase. *Journal of Geophysical Research: Space Physics*, 126, e2021JA029111. [https://](https://doi.org/10.1029/2021JA029111)  
588 [doi.org/10.1029/2021JA029111](https://doi.org/10.1029/2021JA029111)
- 589 Mauk, B. H., Fox, N. J., Kanekal, S. G., Kessel, R. L., Sibeck, D. G., & Ukhorskiy, A.  
590 (2013), Science objectives and rationale for the radiation belt storm probes mission. *Space*  
591 *Science Reviews*, 179, 3–27. <https://doi.org/10.1007/s11214-012-9908-y>
- 592 Miyoshi, Y., Shinohara, I., Takashima, T., Asamura, K., Higashio, N., Mitani, T., et al.  
593 (2018), Geospace exploration project ERG. *Earth Planets Space*, 70, 101.  
594 <https://doi.org/10.1186/s40623-018-0862-0>
- 595 Nuttall, A. (1981), Some windows with very good sidelobe behavior. *IEEE Transactions*  
596 *on Acoustics, Speech, and Signal Processing*, 29(1), 84–91.  
597 <https://doi.org/10.1109/TASSP.1981.1163506>
- 598 Thomson, W.E. (1949), Delay Networks having Maximally Flat Frequency  
599 Characteristics. *Proceedings of the Institution of Electrical Engineers, Part III, Radio and*  
600 *communication engineering*, 96 (44), 487–490. <https://doi.org/10.1049/pi-3.1949.0101>
- 601 Tukey, J. W. (1967), An introduction to the calculations of numerical spectrum analysis.  
602 In B. Harris (Ed.), *Spectral Analysis of Time Series* (pp. 25–46). New York, NY: Wiley.
- 603 Tukey, J. W., & Hamming, R. W. (1949), *Measuring noise color 1*. Murray Hill, NJ: Bell  
604 Telephone Laboratories, Incorporated.
- 605  
606  
607  
608



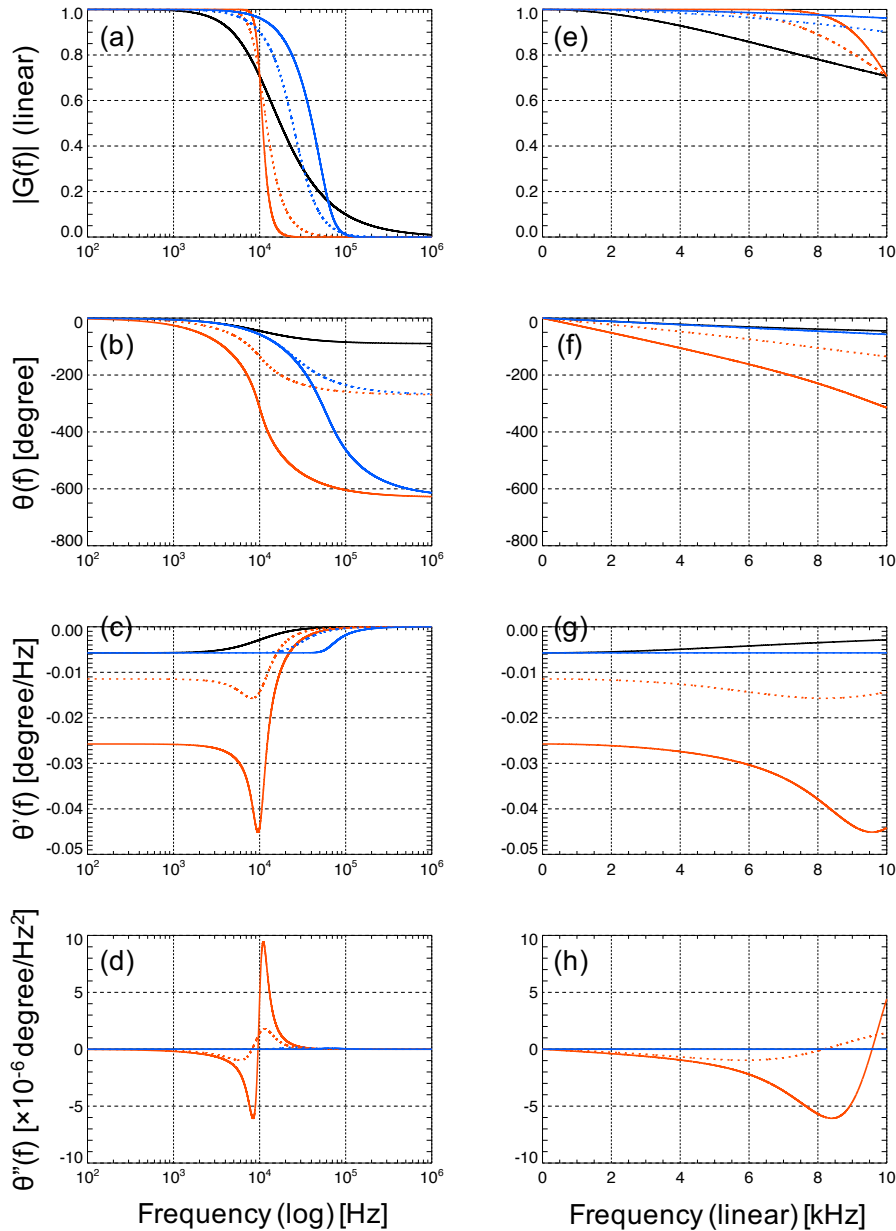
609  
 610 **Figure 1.** Summary plot of (a, c, and e) window functions and (b, d, and f) their frequency  
 611 characteristics. (a, b) the cosine-sum windows: black, red, yellow, green, and blue lines  
 612 correspond to the rectangular, Hamming, Hann, Blackman, and Blackman-Harris window,  
 613 respectively. (c, d) the Tukey-type windows: black, red, yellow, green, and blue lines correspond  
 614 to the rectangular, Tukey-Hamming, Tukey-Hann, Tukey-Blackman, and Tukey-Blackman-  
 615 Harris window, respectively. All windows are plotted with  $r = 0.3$ . (e, f) the Tukey-Hamming  
 616 windows: red, yellow, green, cyan, blue, and black lines correspond to  $r = 0.0, 0.2, 0.4, 0.6, 0.8,$   
 617 and  $1.0$ , respectively.  $r = 0$  and  $1$  correspond to the normal Hamming window and the  
 618 rectangular window, respectively.  
 619



620  
621  
622  
623  
624  
625

**Figure 2.** Flowchart of the calibration procedures for the STFT case comprising conventional methods (Method 1 (yellow), 2 (green), and 3 (blue)) and the novel proposed method (Method 4 (red)).

626



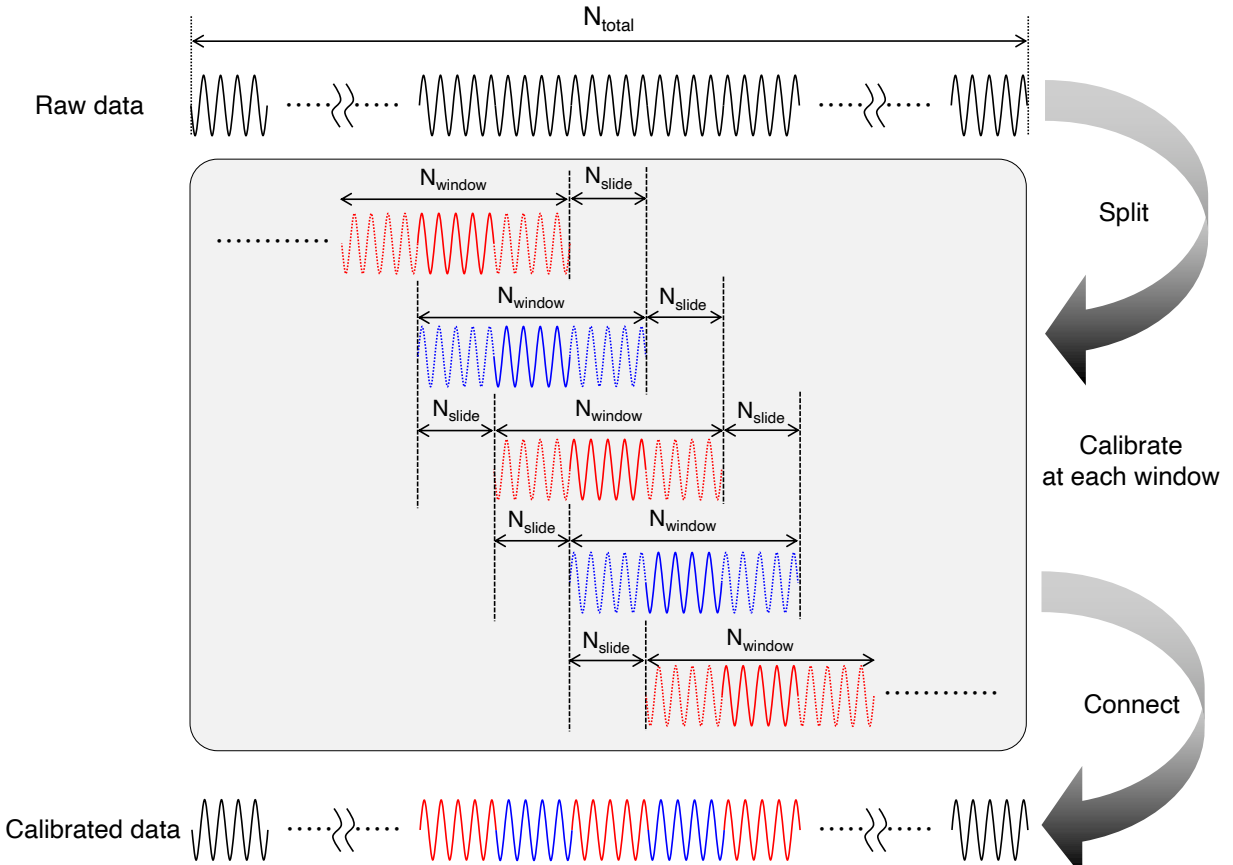
627

628 **Figure 3.** The properties of the filters with  $f_{\text{cutoff}} = 10$  kHz and  $G_0 = 1$ . (a) and (e) are the  
 629 amplitude components of the transfer function  $|G(f)|$  corresponding to the gain of filters, (b)  
 630 and (f) are phase components of the transfer function  $\theta(f)$ , (c) and (g) are the first-order  
 631 derivatives of  $\theta(f)$ , (d) and (h) are the second-order derivatives of  $\theta(f)$ , respectively. Black  
 632 lines, red lines, and blue lines correspond to the RC1, the Butterworth, and the Bessel filters,  
 633 respectively, and dashed and solid red and blue lines correspond to the third- and seventh-order  
 634 filter, respectively.

635

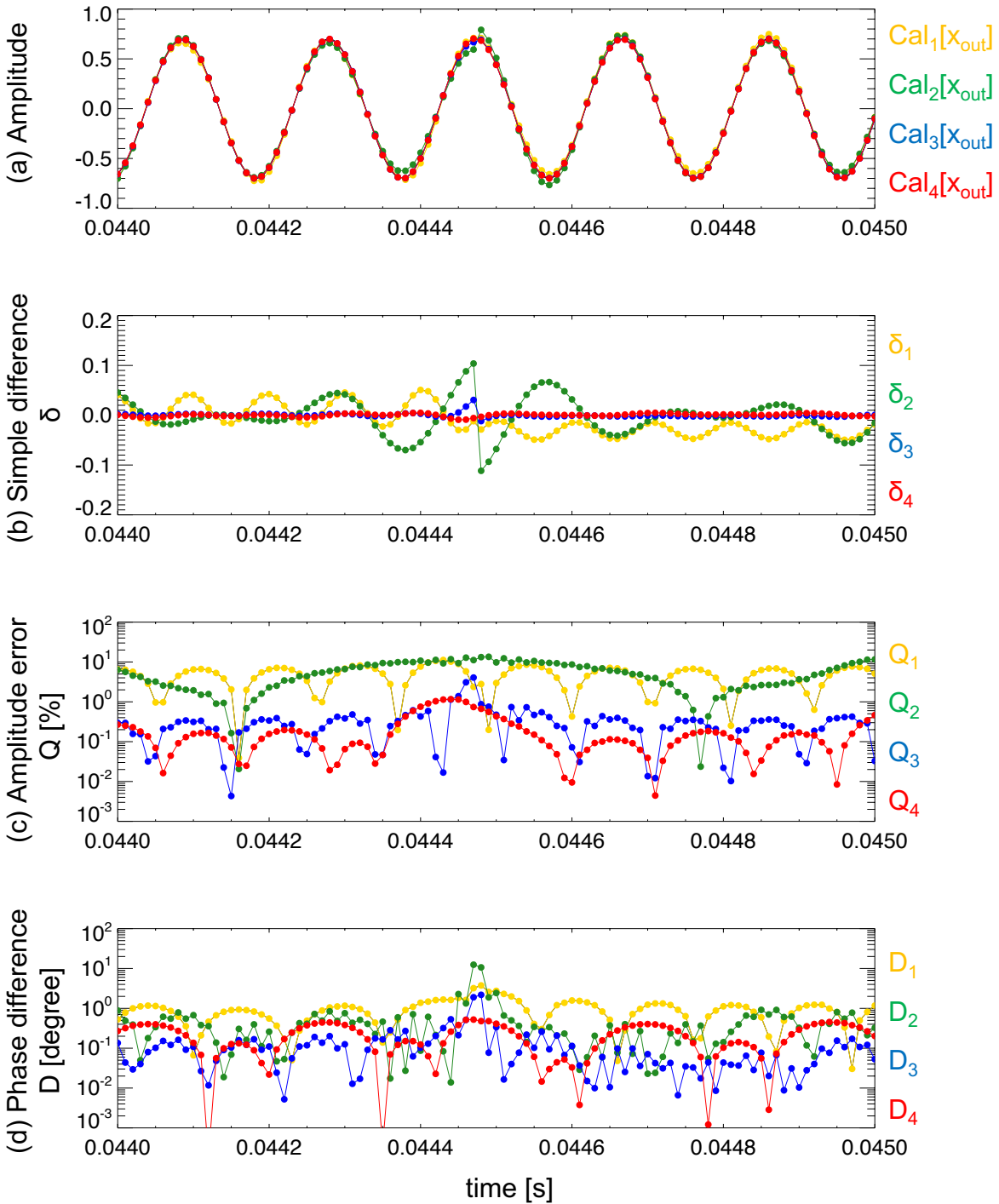
636

637



638  
639  
640  
641

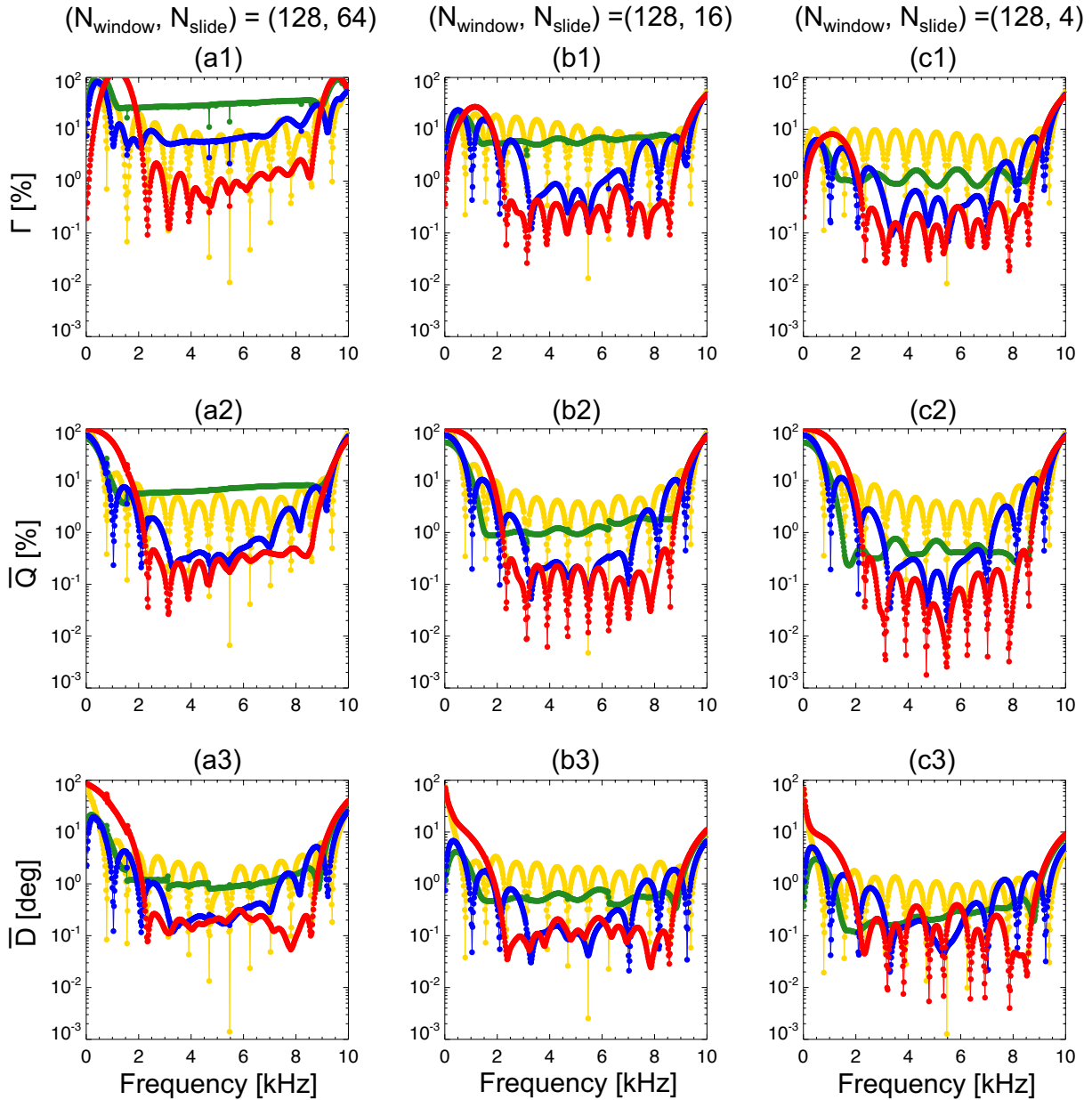
**Figure 4.** Schematic illustration of an STFT process and the definition of  $N_{\text{window}}$ ,  $N_{\text{slide}}$ , and  $N_{\text{total}}$ .



642  
 643  
 644  
 645  
 646  
 647  
 648

**Figure 5.** Sample plot of (a)  $Cal_h[x_{out}(t_n)]$ , (b)  $\delta_h$ , (c)  $Q_h(t_n)$ , and (d)  $D_h(t_n)$  for the third-order Butterworth filter with  $f_s = 100$  kHz,  $N_{total} = 10,000$ ,  $T_{total} = 0.1$  s,  $N_{window} = 128$ ,  $N_{slide} = 64$ ,  $f_{in} = 5.17$  kHz. The data around center are plotted. The yellow, green, blue, and red points and lines correspond to Method 1, 2, 3, and 4, respectively. Note that the input amplitude is 0.7.

### 3rd order Butterworth filter



650

651 **Figure 6.** The frequency dependences of  $\Gamma_h$ ,  $\bar{Q}_h$ , and  $\bar{D}_h$  for the third-order Butterworth filter.

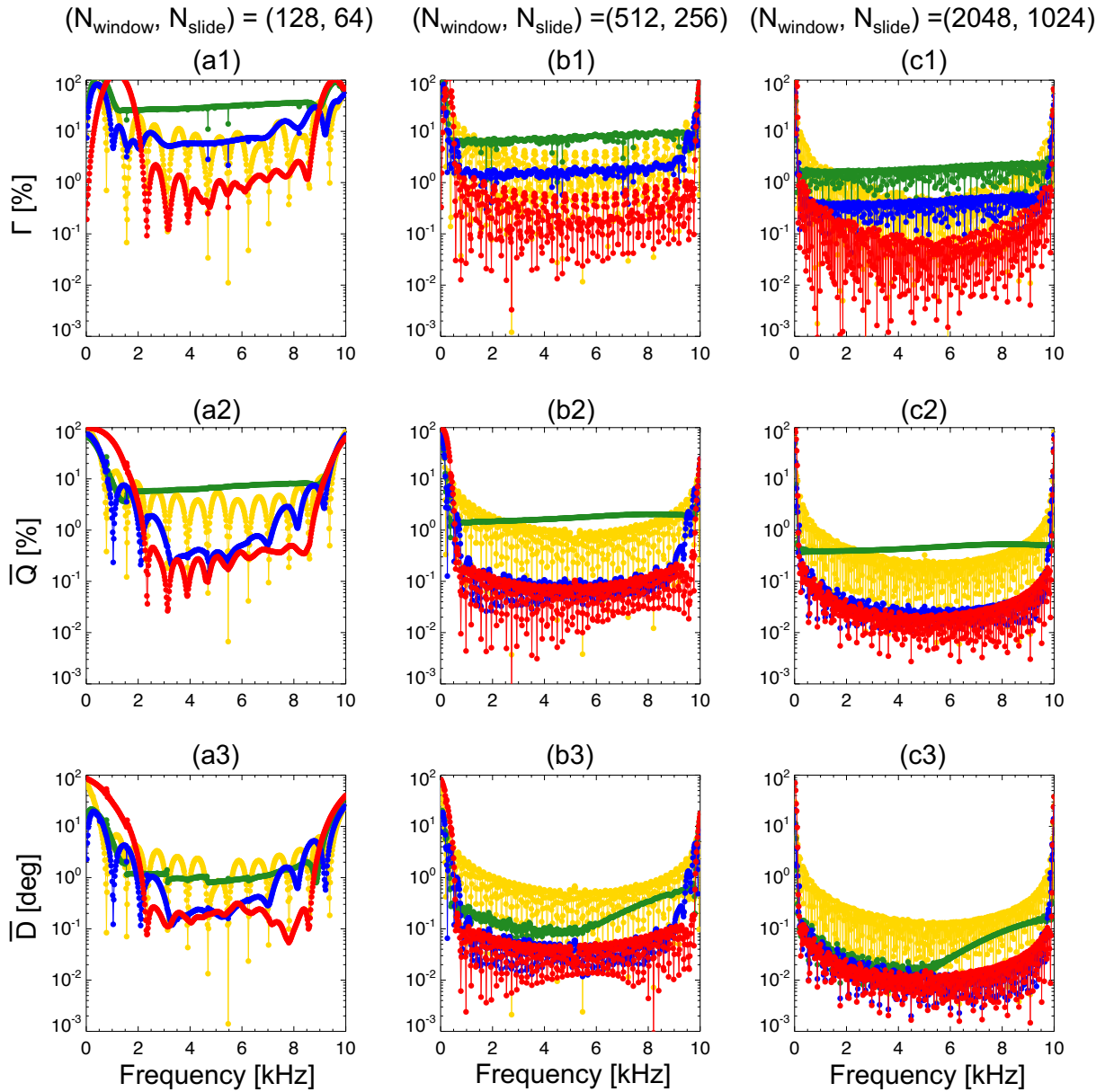
652 (a1-a3) ( $N_{\text{window}}, N_{\text{slide}} = (128, 64 (= N_{\text{window}}/2))$ ), (b1-b3) ( $N_{\text{window}}, N_{\text{slide}} =$

653 ( $128, 16 (= N_{\text{window}}/8)$ ), (c1-c3) ( $N_{\text{window}}, N_{\text{slide}} = (128, 4 (= N_{\text{window}}/32))$ ). The color

654 format is the same as that of Figure 5.

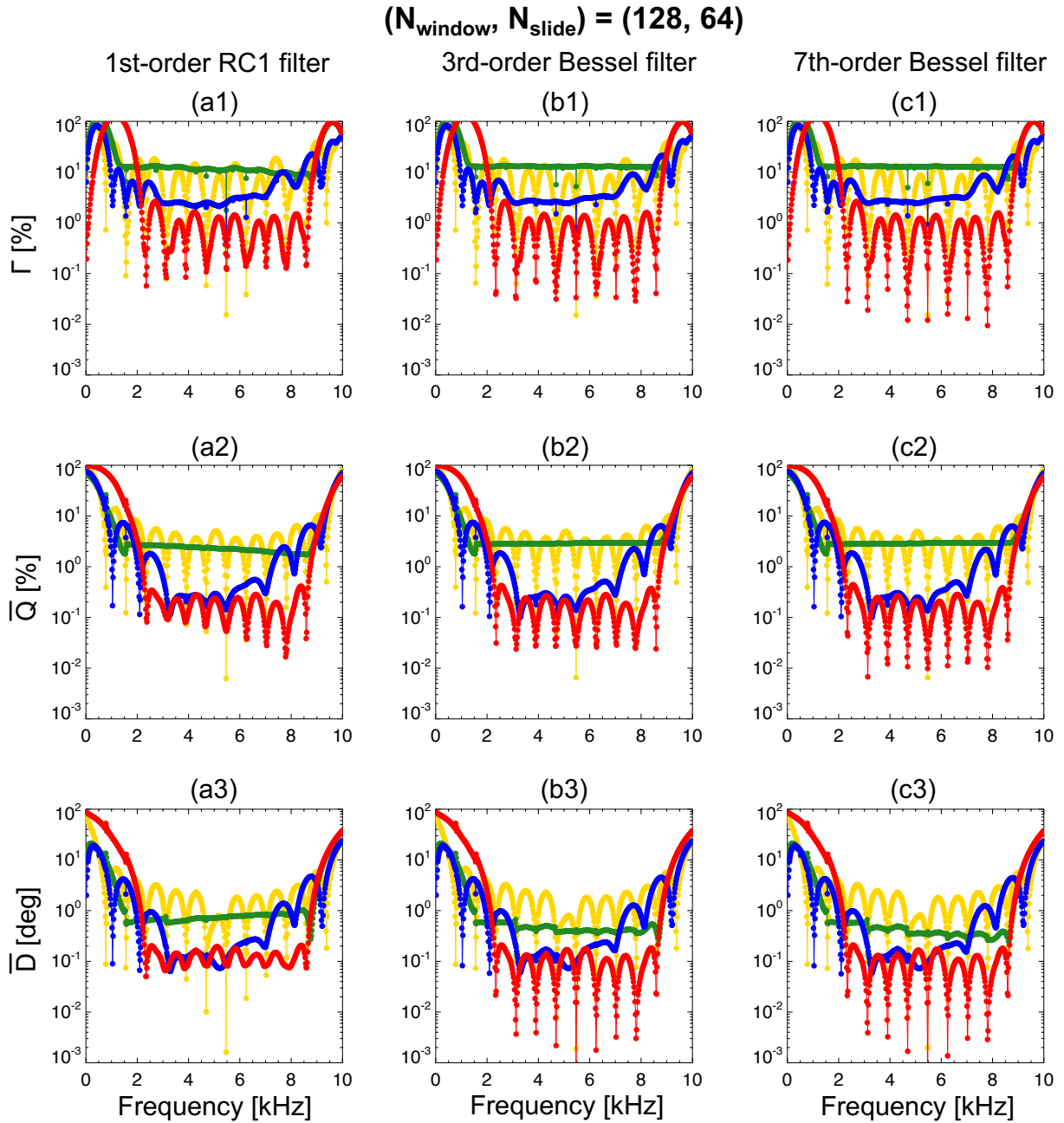
655

**3rd order Butterworth filter**



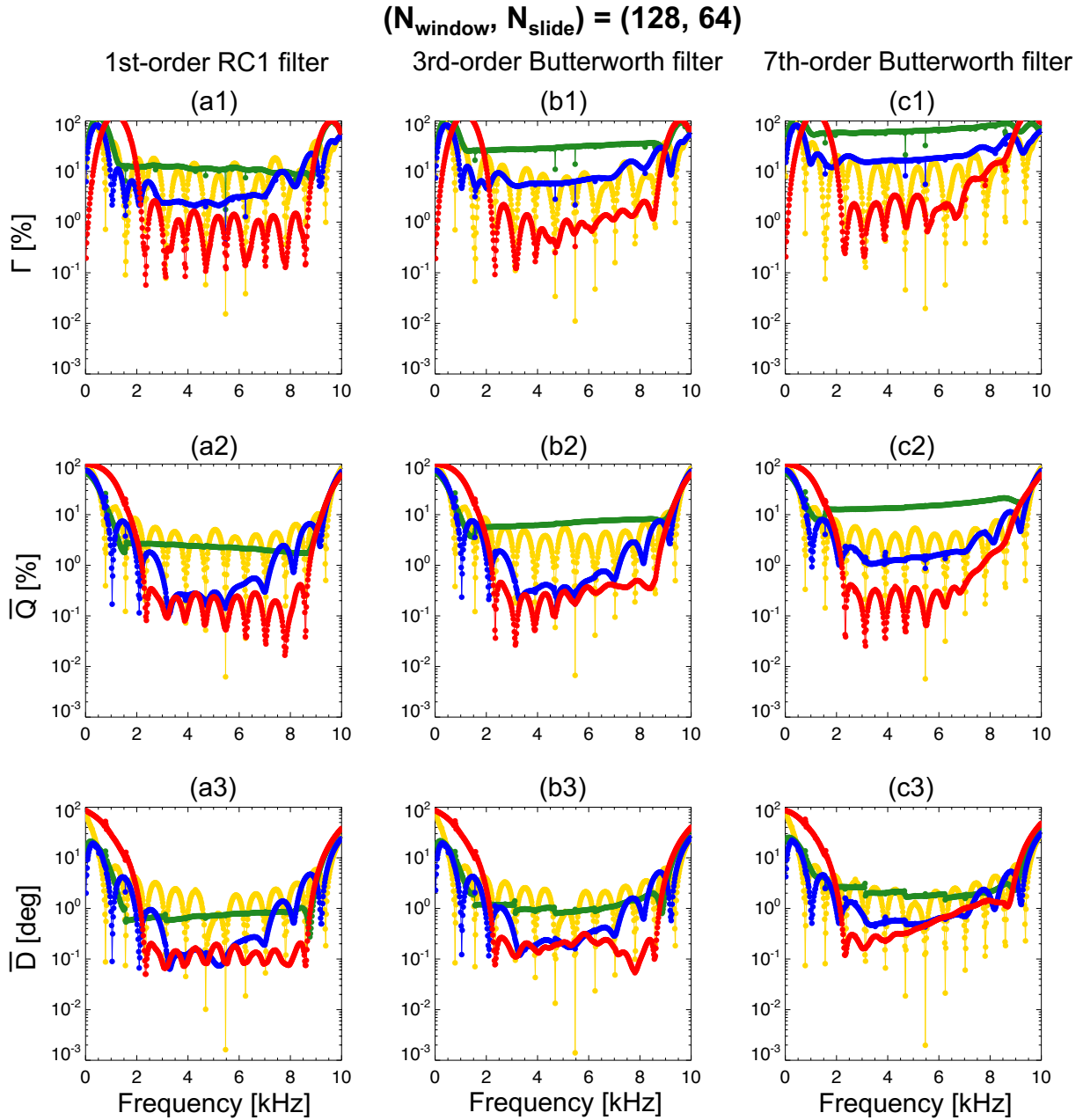
656  
 657 **Figure 7.** The frequency dependences of  $\Gamma_h$ ,  $\bar{Q}_h$ , and  $\bar{D}_h$  for the first-order RC filter. (a1-a3)  
 658  $N_{\text{window}} = 128$ , (b1-b3)  $N_{\text{window}} = 512$ , and (c1-c3)  $N_{\text{window}} = 2048$  with  
 659  $N_{\text{slide}}/N_{\text{window}} = 0.5$ . The color format is the same as that of Figures 5 and 6.

660  
 661



662  
663  
664  
665  
666  
667  
668

**Figure 8.** The frequency dependences of  $\Gamma_h$ ,  $\bar{Q}_h$ , and  $\bar{D}_h$  with  $(N_{\text{window}}, N_{\text{slide}}) = (128, 64)$  for (a1-a3) the first-order RC filter, (b1-b3) the third-order Bessel filter, (c1-c3) the seventh-order Bessel filter. The color format is the same as that of Figures 5, 6, and 7.



669  
670  
671  
672  
673  
674

**Figure 9.** The frequency dependences of  $\Gamma_h$ ,  $\bar{Q}_h$ , and  $\bar{D}_h$  with  $(N_{\text{window}}, N_{\text{slide}}) = (128, 64)$  for (a1-a3) the first-order RC filter, (b1-b3) the third-order Butterworth filter, and (c1-c3) the seventh-order Butterworth filter. The color format is the same as that of Figures 5, 6, 7, and 8.

675  
676  
677  
678

**Table 1.** Summary of characteristics of each calibration method.  $N_t$ ,  $N_w$ ,  $N_s$ , and  $\text{ld}(x)$  represent  $N_{\text{total}}$ ,  $N_{\text{window}}$ ,  $N_{\text{slide}}$ , and the binary logarithm function, respectively.

	<b>Method 1</b>	<b>Method 2</b>	<b>Method 3</b>	<b>Method 4</b> (Our proposed method)
<b>For removing side-lobe effect</b>	Poor	Excellent	Good	Excellent
<b>For removing main lobe effect</b>	Excellent	Poor	Good	Excellent
<b>Accuracy</b>	Poor (Sometimes Excellent)	Poor	Good	Excellent
<b>Seamlessness</b>	Poor	Poor	Good (Sometimes Poor)	Excellent
<b>Calculation time</b>	$\mathcal{O}\left(\frac{N_t N_w \text{ld}(N_w)}{N_s}\right)$	$\mathcal{O}\left(\frac{N_t N_w \text{ld}(N_w)}{N_s}\right)$	$\mathcal{O}\left(\frac{N_t N_w \text{ld}(N_w)}{N_s}\right)$	$\mathcal{O}\left(\frac{N_t N_w^2}{N_s}\right)$

679